# Quantifying Plasma Collision Processes in Xenon Powered Electric Propulsion Systems

Rainer A. Dressler[a] and Yu-hui Chiu[b]

*a) Spectral Sciences, Inc., 4 Fourth Ave, Burlington, MA 01803-3304*
*b) Air Force Research Laboratory, Space Vehicles Directorate, Hanscom AFB, MA 01731-3010*

**Abstract.** The use of xenon plasma electrostatic space propulsion systems for low-thrust applications is growing rapidly due to the significant propellant mass savings associated with the high specific impulse of the engines. The high expense of the propellant drives the cost of ground-based testing, which lacks many attributes of in-space conditions. The cost-effective performance and integration optimization of these propulsion systems, consequently, is highly dependent on models that correctly render the static plasma properties and its outflow from the engine at arbitrary conditions. A primary impediment to the accuracy of models is quantitative data such as energy dependent cross sections for a multitude of collision processes that govern the plasma properties. We present a review of theoretical and experimental advances in determining vital cross sections and their implementation in models of electrostatic thruster plasmas. Experimentally validated theoretical charge exchange and xenon ion differential scattering cross sections have led to improved modeling of the angular distribution of Hall Effect thruster plume ion currents. New cross sections for inelastic electron and xenon ion scattering on xenon atoms, including atoms in the $5p^5 6s$ $J=2$ metastable state, have led to the development of a collisional radiative model that predicts local electron temperatures from near-infrared spectral intensities.

**Keywords:** Electric propulsion, Hall thruster, xenon, xenon plasma, charge exchange, elastic scattering, electron impact excitation, plasma radiation, atomic collisions
**PACS:** 34.20.cf, 34.50.Fa, 34.70.te, 34.80.Dp, 52.20.Fs, 52.20.Hv, 52.25.Dg, 52.25.Os, 52.25.Ya, 52.65.Vv, 52.70.Kz, 52.75.Di

## INTRODUCTION

Xenon plasma electrostatic space propulsion engines, including Hall Effect thrusters and gridded ion thrusters, are finding increased use in low-thrust applications in space. In these engines, expelled xenon ions define the mass flow. Electrostatic acceleration of the ions results in high exit velocities, which define the specific impulse of the engine. The specific impulse also represents the thrust per unit mass flow, and thus the propellant mass utilization efficiency of the engine. Consequently, the high specific impulses in electrostatic electric propulsion engines imply substantial propellant mass savings over chemical engines for a specific mission, defined by the overall change in velocity imparted to the spacecraft ($\Delta v$). Xenon is usually the propellant of choice since it provides a compromise between specific impulse and thrust that suits a broad range of missions. In addition, the relatively low ionization potential of xenon results in a high ionization efficiency at electric powers available in space.

Engineering research and development on xenon-propelled electric propulsion thrusters seeks to improve general performance and electric efficiency of a thruster model. An equally important goal is to integrate the thruster on a spacecraft in a way that minimizes the impact of the engine and its effluents on spacecraft systems. The research relies on ground-based testing, which is expensive due to the high cost of xenon, and which lacks many attributes of in-space conditions. The cost-effective performance and integration optimization of these propulsion systems, consequently, is highly dependent on computational modeling efforts that can forecast the performance of the system in space conditions. The models rely on quantitative data on xenon plasma collision processes such as energy dependent cross sections for electron impact excitation of xenon atoms or xenon ion scattering on xenon atoms.

The most relevant xenon electrostatic thruster plasma collision processes can be summarized as follows:

| | | | | |
|---|---|---|---|---|
| $e^- + Xe$ | $\rightarrow$ | $Xe + e^-$ | Inelastic/Elastic | (1) |
| | $\rightarrow$ | $Xe^{n+} + (n+1)e^-$ | | (2) |
| $e^- + Xe^+$ | $\rightarrow$ | $Xe^{n+} + ne^-$ | Inelastic/Elastic | (3) |
| $Xe^{n+} + Xe$ | $\rightarrow$ | $Xe^{n+} + Xe$ | Inelastic/Elastic | (4) |
| | $\rightarrow$ | $Xe + Xe^{n+}$ | CEX, Inelastic/Elastic | (5) |
| | $\rightarrow$ | $Xe^{n-m+} + Xe^{m+}$ | CEX, Inelastic | (6) |

Electron impact scattering processes (1-3) are associated with electron momentum transfer (elastic scattering), and Xe atom or ion excitation and ionization (inelastic scattering). The inelastic processes are the main source of plasma radiance. As discussed later, metastable atoms or ions can play a fundamental role in the plasma kinetics. The heavy particle collisions (4-6), including processes involving doubly charged ions which are approximately 10% of all ions in the plasma, govern the final spatial velocity distribution of the accelerated ions. Cross sections for these processes are, therefore, crucial in quantitatively modeling ion currents that could lead to material sputtering, either within the engine or on external surfaces of the host spacecraft. Charge exchange (CEX, processes 5 and 6) play a particularly unique role in the plasma dynamics as well as in atomic collision physics. CEX provides a mechanism for dramatically changing the momentum of ions, and is the source of low energy ions near the thruster exit plane that can be accelerated back to the spacecraft.[1, 2] Heavy particle collisions, as demonstrated below, can also contribute to radiance.

In this review we summarize recent advances made in determining absolute cross sections for a number of the processes listed above. We begin with measurements and calculations of charge exchange and elastic differential cross sections (processes 4-6). These results have led to the correct modeling of ion angular distributions, and to predictions of sputtering currents for both singly and doubly charged ions present in the thruster plume. We then proceed with a review of the development of a xenon electrostatic thruster plasma radiative model. This model required a comprehensive set of electron excitation cross sections, in particular cross sections for Xe $5p^5 6s$ $J=2$ metastable atoms. The performance of the model is demonstrated in its ability to extract plasma electron temperatures from passive observation of emission spectra.

## XENON ION SCATTERING STUDIES

### Charge Exchange Cross Sections

Two types of CEX collisions occur in the plasmas of an electrostatic thruster. The first are symmetric CEX collisions (process 5), where the charge state of the colliding atoms is swapped. The second type involves an asymmetric exchange of charge producing new charge states (process 6). These types can be clarified by the example of collisions between doubly charged xenon ions and xenon atoms:

$$Xe^{2+} + Xe \rightarrow Xe + Xe^{2+} \quad (7)$$

$$\rightarrow Xe^+ + Xe^+ \quad (8)$$

CEX collision (7) is a symmetric case where two electrons are transferred from the neutral Xe atom to the ion. Symmetric CEX collisions have large cross sections because they mostly occur without transfer of translational energy. Zero translational energy transfer (i.e., no ion or neutral electronic excitation occurs) corresponds to an elastic collision. In CEX collision (8) a single electron is transferred from the neutral to the ion. This is an asymmetric CEX case accompanied with translational energy transfer unless an accidental resonance exists between reactant and product states. For reaction (8) involving ground state reactants and products, the reaction is accompanied by 8.8 eV of excess kinetic energy (corresponding to the difference between the two-electron ionization energy and two single ionization energies of xenon). Cross sections in asymmetric cases tend to be significantly lower. Furthermore, processes (7) and (8) have entirely different cross section energy dependences due to different CEX mechanisms.

The large cross sections of tens of square-Ångstrom at ion energies of hundreds of electron-volts for symmetric systems implies that the electron hop occurs at long range where the interaction between collision pairs is weak in comparison to the collision translational energy. Consequently, in most symmetric CEX collisions, scattering angles are very small and momentum transfer is negligible. Thus, a fast ion colliding with a stationary neutral atom leads to a stationary ion and a fast neutral. Minor fields (e.g., due to the space charge potential) can then direct the low-energy ions out of the accelerated exhaust beam. CEX, consequently, is an important loss mechanism of accelerated plasma, and can lead to significant redirected ion currents that lead to problems such as insulator erosion within the

engine, and ion currents on sensitive surface of the spacecraft. Accurate CEX cross sections are, therefore, a critical component of thruster integration models.

For Coulomb collisions (for example the reverse of Processes 6 and 8), CEX products with new energies per unit charge are formed. Structure in the energy distribution of Hall thruster plume ions have been attributed to Coulomb CEX collisions.[3] No experimental data is known to us for xenon ion Coulomb CEX collisions in the energy range of interest. Coulomb collisions will not be further discussed in this review, although the theoretical methods discussed below are amenable to Coulomb collisions with some added complications.

Sakabe and Izawa[4] reviewed past experimental work for $Xe^+$ + Xe CEX cross sections. They also report computed cross sections based on a time-dependent, linear combination of atomic orbitals (LCAO) approach. The comparison of the various measurements exhibited significant discrepancies, leading to different values applied in different thruster models. The most commonly used values were based on a model introduced by Rapp and Francis[5] for symmetric CEX of singly charged ions. This model is based on the impact parameter approach for the symmetric CEX cross sections, $\sigma_{CEX}$:

$$\sigma_{CEX} = 2\pi \int_0^\infty P_{CEX}(b) b db \tag{9}$$

where $b$ is the impact parameter which corresponds to the closest distance of approach in a straight-line trajectory, and $P_{CEX}(b)$ is the impact-parameter dependent charge exchange probability. Symmetric CEX is an adiabatic process which occurs when the collision pair is temporarily a molecule, $Xe_2^+$, and the electron to be transferred is no longer in an atomic orbital associated with the electron motion around one nucleus, but a molecular orbital governing motion around both nuclei. Molecular orbital principles state that a symmetric ion pair like $Xe_2^+$ produces pairs of *gerade* and *ungerade* molecular states that differ by the electron exchange interaction. It has been shown that the CEX probability can then be obtained from the elastic scattering phase shifts associated with scattering on the *gerade* and *ungerade* states,[6] $\eta_g(b)$ and $\eta_u(b)$:

$$P_{CEX}(b) = \sin^2\{\eta_g(b) - \eta_u(b)\}. \tag{10}$$

The impact parameter dependent CEX probability is, therefore, an oscillatory function between 0 and 1 up to a specific impact parameter where the probability approaches zero asymptotically as the phase shift difference approaches zero. Rapp and Francis introduced an approximate approach in determining the relevant long-range behavior of the exchange energy, which required only knowledge of the atomic ionization energy. The expression based on a 1-electron LCAO approach for the interatomic potentials $V_g(R)$ and $V_u(R)$ is (atomic units):

$$\text{Rapp and Francis:} \quad V_{g,u}(R) = \pm RI \exp(-\alpha_I R), \tag{11}$$

where $R$ is the interatomic distance, $I$ is the ionization energy, and $\alpha_I = (2I)^{1/2}$. Pullins et al.[7] have pointed out, however, that the expression by Rapp and Francis has an algebraic error, and derived a corrected expression:

$$\text{Pullins et al.:} \quad V_{g,u}(R) = \pm \frac{4}{3} RI \exp(-\alpha_I R). \tag{12}$$

The significantly higher exchange energy leads to substantially higher CEX cross sections. A more rigorous treatment of $H_2^+$ (the basis of the previous approximation) leads to a minor modification of Eq. (12):[8, 9]

$$V_{g,u}(R) = \pm \frac{4}{e} RI \exp(-\alpha_I R). \tag{13}$$

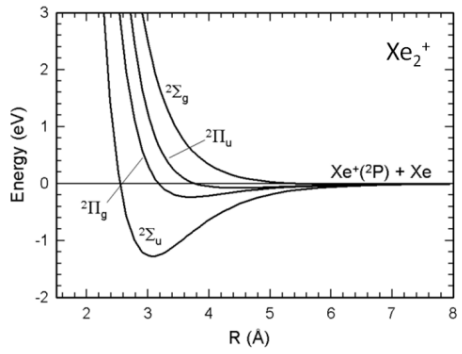


**FIGURE 1:** Spin-Orbit free $Xe_2^+$ interaction potentials computed by Paidarova and Gadea.[9]

The ultimate accuracy is obtained if precise interaction potentials are available, either from quantum chemical calculations or spectroscopic studies. Figure 1 shows the most recently computed spin-orbit free potentials for the $Xe_2^+$ molecular ion.[10] Refinements of these potentials have been derived from recent spectroscopic work.[11] Use of multi-electron potentials of Fig. 1 must take the statistics of the respective potential pairs into account. Equation (9) then needs to be extended to:

$$\sigma_{CEX} = \sum_i d_i \sigma_{CEX,i}, \tag{14}$$

where $d_i$ is a normalized statistical factor for potentials associated with state symmetry, $i$, and $\sigma_{CEX,i}$ are the cross sections associated with scattering on potential pair, $i$. For the $\Sigma$ and $\Pi$ potentials shown in Fig. 1, the statistical factors are 1/3 and 2/3, respectively.

CEX cross sections are measured by passing an energy and mass selected ion beam through a target gas cell at single collision conditions and collecting both primary and CEX ions. The cross section is then given by:

$$\sigma_{CEX} = I_{CEX} / I_{tot} nx, \tag{15}$$

where $I_{CEX}$ is the charge exchange ion current, $I_{tot}$ is the total ion current, $n$ is the neutral target gas density, and $x$ is the effective interaction length. Experiments to determine cross sections over a broad ion energy range are challenging because reactant and products cannot be distinguished mass spectrometrically unless a high resolution mass spectrometer with isotopic resolving power is used. Furthermore, efficient collection is required for ions scattered over broad energy and angular range.

Miller et al.[12] used the guided-ion beam (GIB) method introduced by Teloy and Gerlich[13] to measure CEX cross sections for both singly and doubly charged ions over an ion energy range between 1 and 300 eV per ion charge. A schematic of a GIB experiment is shown in Fig. 2. The mass selected ion beam and scattered ions are confined by inhomogeneous radio-frequency (rf) fields within an octopole ion guide that generate an effective cylindrical potential. The ion energy and ion velocity components with respect to the ion guide axis are fully preserved if the rf frequency is properly chosen. The normal GIB experiment uses a mass filter in conjunction with an electron multiplier or a scintillation detector to record ions. The mass filter, which discriminates mass per unit charge, is not necessary in the present symmetric cases. The main GIB experiment virtue is its accuracy over a very broad range of collision energies.

Miller et al. applied two techniques to distinguish the CEX ions from the otherwise elastically scattered ions. In the first, the attenuation of the beam was measured when the bias potential of the second octopole after the collision region was slightly raised to stop CEX ions with primarily near-thermal energies. In the second, the measurement was conducted with short ion pulses, and the primary and CEX secondary ions were separated through their time of flight. The comparison of both approaches provided a nice crosscheck for accuracy.

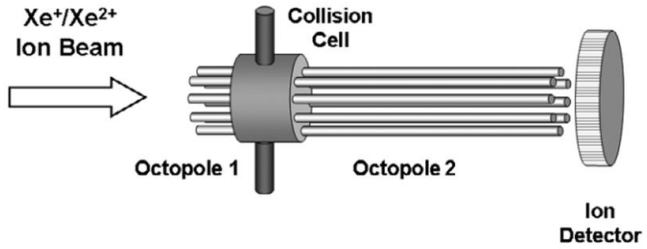


**FIGURE 2:** Schematic representation of a GIB experiment. The ion beam is mass and energy selected. Typically, the ion detector consists of a mass filter and electron multiplier. The mass filter is not needed for the xenon ion symmetric cases.

Figure 3a compares the experimental $Xe^+$ + Xe cross sections by Miller et al.[12] to low-energy drift tube measurements of Okuna et al.[14] and theoretical results including predictions by the original Rapp and Francis model, the 1-electron model based on the corrected exchange energy (Eq. 13), and present computations using full spin-orbit potentials by Paidarova and Gadea.[10] The experimental results agree best with the theoretical values based on the *ab-initio* potentials (PG Potential). The values from the corrected 1-electron model, however, are only slightly lower than those of the experiment and the more accurate computation. The Rapp and Francis values are significantly lower than the experimental values, consistent with the underprediction of the exchange energy. From these results, we derive a simple expression for the energy dependence of the CEX cross section for singly-charged ions valid between 1 and ~600 eV:

$$\sigma_{CEX}(Xe^+) = 90.9 - 15.4 \log_{10}(E), \tag{15}$$

where $E$ is the ion energy in units of eV.

Figure 3b shows symmetric and asymmetric CEX cross sections for $Xe^{2+}$ + Xe collisions. For the symmetric cross sections, the GIB data[12] is compared with drift tube data by Okuno et al.[14] The solid line is the 1-electron model calculation where the 2-electron ionization is used for $I$. Both experimental and theoretical data are in good agreement given the experimental uncertainties which are typically quoted at 30%. Particularly remarkable is the agreement between the drift tube data and theory at low energies. The asymmetric cross sections are significantly lower than the symmetric values and exhibit threshold-like behavior, despite the fact that lower-energy products are formed. This is consistent with a non-adiabatic mechanism involving potential curve crossings. From the experimental data, we derive a simple expression for the cross sections between 2 and ~1,000 eV:

$$\sigma_{CEX}(Xe^{2+}) = 45.7 - 8.9 \log_{10}(E) \tag{16}$$

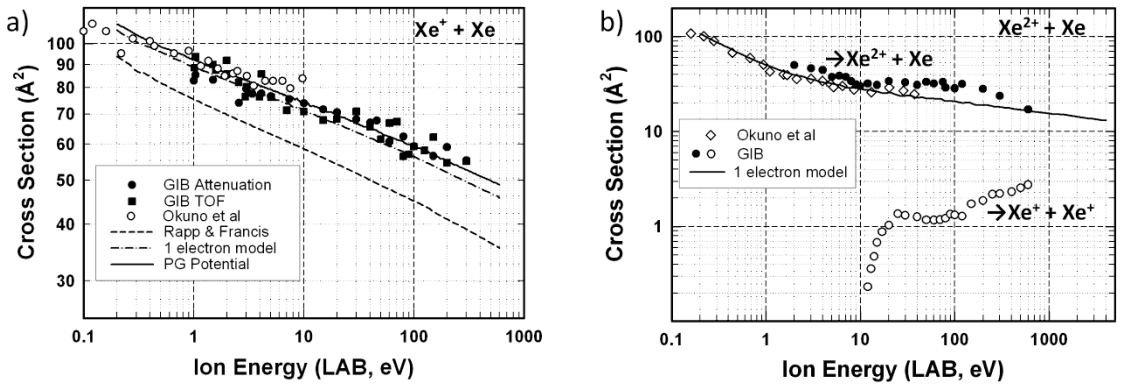


**FIGURE 3:** a) Experimental and theoretical $Xe^+ + Xe$ symmetric CEX cross sections. b) Experimental and theoretical $Xe^{2+} + Xe$ symmetric and asymmetric CEX cross sections. GIB values first reported by Miller et al.[12]

## Differential Scattering Cross Sections

Xenon ion differential scattering cross sections in collisions with xenon atoms provide angular scattering information for electrostatic thruster models. Elastic collisions are the main source of angular scattering. Differential elastic scattering cross sections can be readily computed from the classical deflection function:[15]

$$\Theta_{CM}(E_T, b) = \pi - 2b\int_{R_0}^{\infty} \frac{dR}{R^2[1 - b^2/R^2 - V(R)/E_T]^{1/2}} \tag{16}$$

where $E_T$ is the translational energy or center-of-mass collision energy, and $R_0$ is the turning point or closest point of approach of the trajectory. Thus, knowledge of the interaction potential, $V(R)$, is sufficient to determine elastic differential cross sections, $d\sigma/d\Omega_{CM}$, where $d\Omega_{CM}$ is the solid angle $2\pi|\Theta_{CM}|d|\Theta_{CM}|$ and $\Theta_{CM}$ is the center-of-mass scattering angle. The cross sections of interest are those specific to ion scattering, and symmetric CEX must be taken into account through the transformation:

$$d\sigma_{CEX}(\theta_{CM})/d\Omega_{CM} = (1 - P_{CEX}(\theta_{CM}))d\sigma(\theta_{CM})/d\Omega_{CM} + P_{CEX}(\theta_{CM})d\sigma(\pi - \theta_{CM})/d\Omega_{CM}. \tag{17}$$

Since the charge-exchange probability, $P_{CEX}(\theta_{CM})$, is highly oscillatory between 0 and 1 at significant scattering angles, and, thus averages to $P_{CEX}(\theta_{CM})$=0.5, Eq. (17) can be simplified to:

$$d\sigma_{CEX}(\theta_{CM})/d\Omega_{CM} = \tfrac{1}{2}d\sigma(\theta_{CM})/d\Omega_{CM} + \tfrac{1}{2}d\sigma(\pi - \theta_{CM})/d\Omega_{CM}. \tag{18}$$

Classically determined differential cross sections for $Xe^+ + Xe$ scattering were successfully applied by Boyd and Dressler[16] in a direct simulation Monte Carlo (DSMC) particle in cell (PIC) model to reproduce the angular extent of a Hall thruster plume characterized in space and by Mikellides et al.[17] using a LaGrangian fluid model to reproduce the angular dependence of exhaust ion energy distributions measured in a ground-based test facility.

The work by Boyd and Dressler and Mikellides et al did not account for doubly charged ions, constituting about 10% of all ions. Since the kinetic energy of scattered doubly charged ions impacting a surface are twice that of singly charged ions following the same trajectory, large $Xe^{2+} + Xe$ elastic scattering differential cross sections would mean that doubly charged ions cannot be neglected when determining surface erosion rates due to sputtering. Accurate $Xe^{2+} + Xe$ interaction potentials such as those in Fig. 1 are not available, thereby preventing the theoretical determination of differential cross sections. Until recently, no measurements have been conducted on $Xe^{2+} + Xe$ elastic scattering differential cross sections at large angles and at the energies of interest.

Chiu et al.[18] applied the GIB method to determine an effective interaction potential for $Xe^{2+} + Xe$ collisions. Contrary to crossed-beam experiments, the traditional experiment for elastic scattering studies, the GIB technique can determine absolute differential cross sections.[19] The angular resolution is not as high as for the crossed-beam experiments. However, Chiu et al. overcame this problem by determining an analytical functional form of the scattering potential that reproduces the observed axially projected ion velocity distributions with elastic scattering simulations. Examples of their measurements and computations are shown in Fig. 4. The experimental differential cross sections are plotted as axially projected ion velocity distributions obtained from velocity transformed ion time-of-flight spectra. Their methodology was validated on the $Xe^+ + Xe$ system using the potentials of Fig. 1. Figure 4a) shows a projected velocity distribution for 20 eV ions where the solid circles are the experimental data, and the solid line is the model distribution on an absolute differential cross section scale. The peak at low velocities is

primarily due to CEX ions. Large-angle scattered ions appear near $v_{CM}$ (half the beam ion velocity). The excellent agreement between experiment and model at these velocities confirms the accuracy of the differential cross sections obtained using the potentials by Paidarova and Gadea[10] (Fig. 1) and the expressions above.

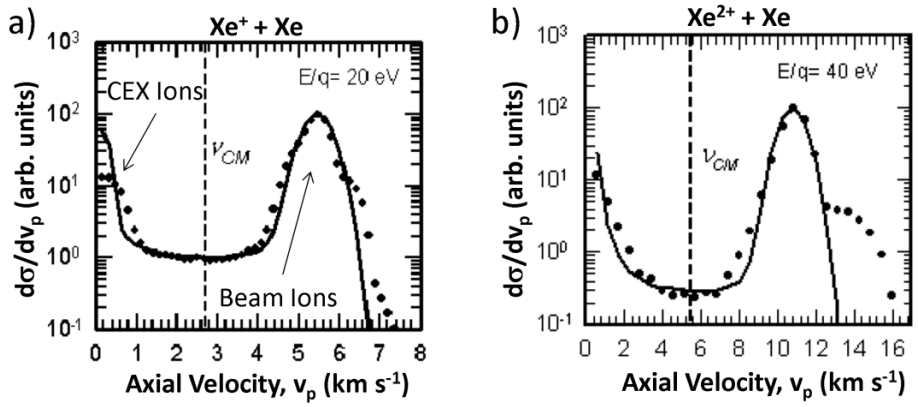


FIGURE 4: GIB measurements (solid circles) and modeled axial ion velocity distributions (solid line) for a) $Xe^+$ + Xe scattering at E/q=20 eV and b) for $Xe^{2+}$ + Xe scattering at E/q=40 eV.

Figure 4b) is a corresponding projected axial velocity distribution for $Xe^{2+}$ ions with a beam energy of 40 eV per unit charge. The high-velocity shoulder of the beam peak can be attributed to the asymmetric singly charged ion products, which are not discriminated against in the experiment. Chiu et al. conducted similar measurements for a series of ion energies, and a potential was determined that best reproduced the large-angle scattering intensities (signal near $v_{CM}$ in Fig. 4b) at all energies. The solid line in Fig. 4b was modeled using following analytical potential expression consisting of a combination of a Morse and a repulsive potential:

$$V_{Xe^{2+}}(R) = 0.006\{\exp(0.544(11.4-R)) - 2\exp(0.272(11.4-R)\} + 1{,}500\exp(-3.737R) \qquad (19)$$

where all parameters are provided in atomic units.

While the above treatment is carried out in the center-of-mass (CM) frame of reference, the energy of ions affecting spacecraft surfaces off the thrust axis are governed by momentum transfer in a laboratory (LAB) or spacecraft frame of reference. The elastic scattering coordinate systems are clarified by a Newton diagram in Fig. 5a), where CM and LAB velocity vectors of scattered particles are designated with $u'$ and $v'$, respectively. Figure 5b) plots laboratory frame $Xe^+$ + Xe and $Xe^{2+}$ + Xe elastic scattering differential cross sections, $d\sigma/d\Omega_{CM}$, computed for $E/q$ = 270 eV, the plume average ion energy of a 300 V Hall thruster. The cross sections are obtained from the potentials in Fig. 1, the potential function (19), and by applying the appropriate coordinate transformation Jacobian.

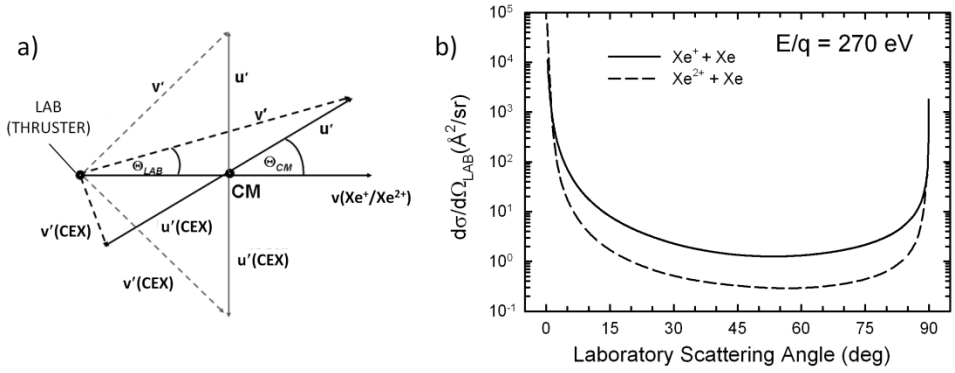


FIGURE 5: a) Newton diagram for center-of-mass (CM) and laboratory/thruster (LAB) coordinates. u´ and v´ are scattered CM and LAB velocity vectors, respectively. b) LAB differential cross sections for $Xe^+/Xe^{2+}$ + Xe collisions at $E/q$ = 270 eV.

The cross sections in Fig. 5b show that the doubly charged ion differential cross sections are significantly lower than those for the singly charged ions at the same $E/q$. Chiu et al.[18] used the differential cross sections to estimate sputtering yields as a function of scattering angle. They determined that at angles below 45°, approximately 10 to 20% of the sputtering is due to doubly charged ions for a typical ion charge ratio of $Xe^{2+}/Xe^+$ =0.1. At larger angles, the doubly-charged ion contribution increases to above 50% at 70°.

## EXCITATION CROSS SECTIONS FOR XENON PLASMA RADIATIVE MODELS

Numerous methods are used to diagnose the plasmas of xenon propelled spacecraft engines. Plasma potential and electron temperature data is generally obtained with Langmuir probes, and ion velocity distributions have been measured using laser-induced fluorescence techniques. An attractive, simple and non-intrusive approach is a passive optical probe of the plasma spectral radiance to deduce plasma properties. There have been many efforts to derive plasma parameters from the plasma radiation, which requires a quantitative collisional radiative model that incorporates all the excitation and de-excitation processes. The primary obstacle to developing such a model has been the lack of vital cross sections. Fons and Lin[20] and Chiu et al.[21] demonstrated that both relative and absolute intensities of Xe I near-infrared (NIR) lines, observed in single collision electron emission excitation spectra exhibited a marked dependence on the electron energy. These authors reported electron emission excitation cross sections over a broad energy range. Crucial for the development of a simple model was the fact that the emission excitation cross sections included cascading, thus eliminating the need to incorporate transitions between cascading states that don't emit in the NIR, and, therefore, greatly simplifying the chemical kinetics of the plasma radiance model. In addition, Chiu et al. reported cross sections for NIR line emission excitation by xenon ions at 300 eV per charge. They showed that at low electron temperatures, such as those encountered in the plasma plume, ion emission excitation plays an important role, and that the spectra due to ions had significant differences compared with the electron excited spectra. The NIR spectrum, therefore, promises to have substantial diagnostic value.

Karabadzhak et al.[22] used the cross sections reported by Fons and Lin[20] and Chiu et al.[21] to create a simple collisional radiative model. According to Karabadzhak *et al.* [22], the excitation rate of a particular NIR line at wavelength, λ, in energy units per steradian can then be expressed as:

$$J_\lambda(\mathrm{XeI}) = \frac{hc}{4\pi\lambda} N_0 N_e \left( k_{e0}^{\lambda} + \frac{N_m}{N_0} k_{em}^{\lambda} + \alpha \cdot k_1^{\lambda} + \frac{1-\alpha}{2} k_2^{\lambda} \right) \tag{20}$$

where $N_0$ is the neutral atom number density, $N_e$ is the electron number density, $N_m$ is the metastable atom number density, $\alpha = N_1/N_e$ is the ratio of singly charged ion density to the electron number density, $k_{e0}{}^{\lambda}$ is the ground-state atom electron impact line emission excitation rate coefficient, $k_{em}{}^{\lambda}$ is the metastable-atom electron impact line emission excitation rate coefficient, and $k_1{}^{\lambda}$ and $k_2{}^{\lambda}$ are the singly and doubly charged ion collision emission excitation rate coefficients. Due to the lower emission excitation energies of metastables, most notably the $5p^5 6s$ $J=2$ ($1s_5$ in Paschen notation) state, they can greatly enhance line intensities at low electron temperatures. At the time of the work by Karabadzhak et al., no electron excitation cross section data involving the Xe I $1s_5$ state were available. A model was erected based on an approximate treatment of metastables assuming optical transition selection rules. The final model for 8 NIR transitions was able to retrieve electron temperatures from chamber experimental data that were in reasonable agreement with probe measurements.

Since the model developed by Karabadzhak et al., Jung and coworkers[23] have reported experimental measurements of emission excitation cross sections from the $1s_5$ metastable state. Dressler et al.[24] extended the model to explicitly compute metastable densities using the experimental cross sections as well as newly reported state-of-the-art semi-relativistic Breit-Pauli B-Spline R-matrix and relativistic distorted wave theoretical computations of cross sections for additional excitation and depopulation transitions, most notably optically forbidden transitions involving other Xe I $1s_i$ states.

The resulting model exhibited high fidelity at low electron temperatures (<10 eV). Figure 6 shows a comparison of spectral intensities observed in the plume of a Russian D55 TAL Anode Layer thruster and model fits reported by Dressler et al.[24] for the 8 NIR lines, all of which are associated with different $2p_j$ upper levels. Table 1. compares electron temperatures extracted from spectral data taken from two positions along the thrust axis of the same engine. The extractions used the CRM of Karabadzhak et al. (KCD) and the more recent model by Dressler et al. applying different cross section sets. BSR-RDW uses only theoretical metastable excitation cross sections, while BSR-RDW-Jung uses data from Jung et al.[23] where available. The table also compares temperatures derived from an 8-line analysis to those using a 2-line analysis involving the 823, 828, and 834 nm lines. Also listed are the relative standard deviations for the 8-line analysis. The 3 models produce identical results for the 834/828 2-line extraction because both of these lines are not optically coupled to the $1s_5$ metastable state, and the only difference between the models is how they treat metastables. The 823 nm line, on the other hand, is strongly coupled to the $1s_5$ state. The BSR-RDW models produce consistent electron temperatures at 200 mm from the thruster exit plane. At 25 mm, the respective 823/828 values are significantly lower than the 8-line analysis and the 834/828 values. As seen in Fig. 6, however, the 834 nm line is quite weak making the 834/828 ratio subject to experimental errors. An 8-line analysis is, therefore, recommended for highest accuracy, while a 2-line analysis is attractive for a quick look. Furthermore, the proximity of the recommended line pairs obviates the need for a precise spectral sensitivity calibration.

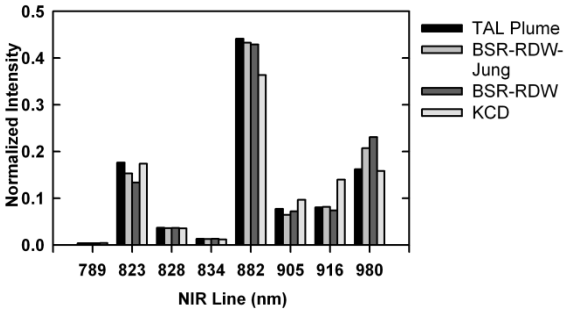


FIGURE 6: Comparison of normalized spectral intensities observed in the plume of a D-55 Xe plasma anode layer thruster (TAL) with model electron temperature fits (see text).

TABLE 1: CRM electron temperatures ($T_e$) obtained from modeling NIR spectral intensities at 200 and 25 mm from the exit plane of a 300 V anode layer thruster. See text.

| | $T_e$ (eV) | | | |
|---|---|---|---|---|
| | 823/828 | 834/828 | 8-line | $\chi$ |
| | | 200 mm | | |
| KCD | 3.4 | 2.8 | 3.4 | 0.284 |
| BSR-RDW-Jung | 2.5 | 2.8 | 2.7 | 0.124 |
| BSR-RDW | 2.3 | 2.8 | 2.6 | 0.176 |
| | | 25 mm | | |
| KCD | 5.6 | 4.8 | 6.1 | 0.318 |
| BSR-RDW-Jung | 3.4 | 4.8 | 4.5 | 0.252 |
| BSR-RDW | 2.8 | 4.8 | 4.6 | 0.302 |

## CONCLUSIONS

The present review provides only a sampler of how atomic and electronic collision cross sections contribute to quantifying models of future electric propulsion engines. Much work is still in progress, such as the determination of Coulomb charge-exchange and electron-ion excitation (process 3) cross sections for modeling the xenon UV-VIS plasma spectrum, and the implementation of a collisional radiative model in three-dimensional engine models.

## ACKNOWLEDGMENTS

The authors wish to acknowledge their colleague at AFRL Hanscom AFB, MA, Dr. Dale J. Levandier, who contributed to many of the projects reviewed in this paper. The authors are also indebted to Drs. Iain Boyd, Dieter Gerlich, George Karabadzhak, C. Y. Ng, Rajesh Srivastava, Klaus Bartschat, Frederic Merkt, Lee Johnson, and Bill Hargus for enlightening collaborations in the research of plasmas of xenon-powered electric propulsion systems. The work conducted at AFRL was supported by AFOSR (Program managers: Michael R. Berman and Kent Miller).

## REFERENCES

1. R. I. Samanta_Roy, D. E. Hastings and N. A. Gatsonis, *J. Spacecraft and Rockets* **33**, 525-534 (1996).
2. R. I. Samanta_Roy, D. E. Hastings and S. Taylor, *J. of Comp. Phys.* **128**, 6-18 (1996).
3. L. B. King and A. D. Gallimore, *Phys. Plasmas* **6**, 2936-2942 (1999).
4. S. Sakabe and Y. Izawa, *Atomic Data and Nuclear Data Tables* **49**, 257-314 (1991).
5. D. Rapp and W. E. Francis, *J. Chem. Phys.* **37**, 2631-2645 (1962).
6. H. S. W. Massey and R. A. Smith, *Proc. Roy. SOc. A* **142**, 142 (1933).
7. S. H. Pullins, R. A. Dressler, R. Torrents and D. Gerlich, *Z. Phys. Chem.* **214**, 1279-1297 (2000).
8. T. C. Scott, J. F. Babb, A. Dalgarno and J. D. Morgan, *J. Chem. Phys.* **99**, 2841-2854 (1993).
9. K. T. Tang, J. P. Toennies and C. L. Yiu, *J. Chem. Phys.* **94**, 7266-7277 (1991).
10. I. Paidarova and F. X. Gadea, *Chem. Phys.* **274** (1), 1-9 (2001).
11. O. Zehnder, R. Mastalerz, M. Reiher, F. Merkt and R. A. Dressler, *J. Chem. Phys.* **128**, 234306 (2008).
12. J. S. Miller, S. H. Pullins, D. J. Levandier, Y. Chiu and R. Dressler, *J. Appl. Phys.* **91** (3), 984-991 (2002).
13. E. Teloy and D. Gerlich, *Chemical Physics* **4**, 417-427 (1974).
14. K. Okuno, T. Koizumi and Y. Kaneko, *Phys. Rev. Lett.* **40**, 1708-1710 (1978).
15. M. Child, *Molecular Collision Theory*. (Academic Press, London, 1974).
16. I. D. Boyd and R. A. Dressler, *J. Appl. Phys.* **92** (4), 1764-1774 (2002).
17. I. G. Mikellides, I. Katz, R. A. Kuharski and M. J. Mandell, *J. of Propulsion and Power* **21** (1), 111-118 (2005).
18. Y. Chiu, R. A. Dressler, C. Houchins and C. Y. Ng, *J. Phys. D: Appl. Phys.* **41**, 165503 (2007).
19. D. Gerlich, *Adv. Chem. Phys.* **82**, 1 (1992).
20. J. T. Fons and C. C. Lin, *Phys. Rev. A* **58**, 4603-4615 (1998).
21. Y. Chiu, B. L. Austin, S. Williams, R. A. Dressler and G. F. Karabadzhak, *J. Appl. Phys.* **99**, 113304 (2006).
22. G. F. Karabadzhak, Y. Chiu and R. A. Dressler, *J. Appl. Phys.* **99**, 113305 (2006).
23. R. O. Jung, T. E. Stone, J. B. Boffard, L. W. Anderson and C. C. Lin, *Phys. Rev. A* **72**, 022723 (2005).
24. R. A. Dressler, Y. Chiu, O. Zatsarinny, K. Bartschat, R. Srivastava and L. Sharma, *J. Phys. D* **42**, 185203 (2009).